

Odd dynamics of passive objects in a chiral active bath

Cory Hargus,¹ Federico Ghimenti,^{1,2} Julien Tailleur,^{1,3} and Frédéric van Wijland¹

¹*Laboratoire Matière et Systèmes Complexes (MSC),*

Université Paris Cité & CNRS (UMR 7057), 75013 Paris, France

²*Department of Applied Physics, Stanford University, Stanford, CA 94305, USA*

³*Department of Physics, Massachusetts Institute of Technology, Cambridge, MA 02139, USA*

When submerged in a chiral active bath, a passive object becomes a spinning ratchet imbued with odd transport properties. In the adiabatic limit of a massive object, we derive the most general Langevin dynamics for a rigid body in a chiral active bath, with odd diffusion and odd mobility connected by an Einstein relation, and numerically explore the breakdown of these predictions beyond the adiabatic limit. We show that the irreversibility of a massive object increases as its symmetry decreases: a disk exhibits an effective equilibrium dynamics, while a rod admits distinct translational and rotational temperatures, and a wedge is fully out of equilibrium. Conversely, this departure from equilibrium can be read in the universal far-field currents and density modulations of the bath, which we measure numerically and derive analytically.

A microscopic object in a fluid bath inherits its dynamics from collisions with the bath particles. When the bath is in equilibrium, the object obeys the Einstein relation and exhibits Boltzmann statistics. Active baths, by contrast, allow a richer set of phenomena and have thus attracted a lot of attention [1–18]. Notable among these is ratchet motion [19–23], which demonstrates how an active bath can power microscopic engines [24–27]. When asymmetric gears are inserted into an active bacterial bath [28–30], rotational ratchet motion arises due to broken time-reversal symmetry of the bath and broken parity symmetry (*i.e.* chirality) of the object.

A chiral active bath, however, breaks both these symmetries by itself, so that even symmetric objects become rotational ratchets [31] imbued with odd diffusivity [32, 33] and odd mobility [34, 35]. While extensive analytical and numerical results are available for achiral baths, little is known theoretically of the dynamics of passive objects embedded in chiral active fluids. The latter are however abundant in both biological [36–38] and synthetic active systems [39]. This raises two key questions: how are the emerging properties of the object (and the bath) interrelated, and how are they influenced by the object shape?

In this Letter, we answer these questions by constructing a general theory to describe the dynamics of a massive object embedded in a chiral active bath. This allows us to show that the object dynamics become increasingly rich as its symmetry decreases. Specifically, we consider the disk, rod, and wedge depicted in Fig. 1. For the disk, we find an effective equilibrium description for the positional degrees of freedom, accompanied by circulating currents in momentum space. The rod already departs thermal equilibrium by featuring unequal effective temperatures for its rotational and positional degrees of freedom. The wedge fully departs from any effective equilibrium and behaves as both a translational and rotational ratchet. Finally, we show how the object shape influences the structure and flow of the bath itself through the generation of density modulations and currents that increase as the object symmetry decreases. Numerical details are

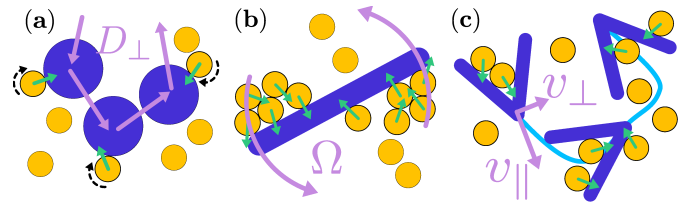


FIG. 1. **Passive objects** inherit chiral dynamics from the bath. A disc (a) exhibits odd diffusivity D_{\perp} , a rod (b) additionally rotates with a ratchet velocity Ω , and a passive wedge (c) additionally translates with ratchet velocities v_{\parallel} and v_{\perp} .

provided in the End Matter.

Model system and effective dynamics. We consider an extended rigid body of arbitrary shape interacting under Hamiltonian dynamics with a chiral active bath in two dimensions. This object has mass M and moment of inertia I . Its state is characterized by its position \mathbf{R} , momentum \mathbf{P} , orientation Θ and angular momentum L . The equations of motion of the object are

$$M\ddot{\mathbf{R}} = \dot{\mathbf{P}} = \mathbf{F}, \quad I\ddot{\Theta} = \dot{L} = \Gamma, \quad (1)$$

where \mathbf{F} and Γ are the total force and torque due to the bath particles. The latter are modeled as chiral active Brownian particles, whose positions \mathbf{r}_i and orientations θ_i evolve as

$$\gamma\dot{\mathbf{r}}_i = \mathbf{F}_i + f_0\mathbf{u}_i + \sqrt{2\gamma D_t}\boldsymbol{\eta}_i, \quad \dot{\theta}_i = \omega_0 + \sqrt{2D_r}\xi_i. \quad (2)$$

Here, γ is the substrate friction, f_0 is the active force oriented along the director $\mathbf{u}_i = [\cos(\theta_i), \sin(\theta_i)]^T$, and object-bath interactions are reciprocal, $\sum_i \mathbf{F}_i = -\mathbf{F}$. The bath displays two active lengthscales: the persistence length $\ell_p = \frac{f_0}{D_r\gamma}$ and gyroradius $\ell_g = \frac{f_0}{|\omega_0|\gamma}$.

If the motion of the object is very slow relative to that of the bath, we can work in the adiabatic limit [17, 40–42] where the probability distribution of the full system factorizes as $\rho(\mathbf{R}, \mathbf{P}, \Theta, L, \mathbf{r}^N, \mathbf{u}^N, t) \approx$

$\rho_o(\mathbf{R}, \mathbf{P}, \Theta, L, t)\rho_b(\mathbf{r}^N, \mathbf{u}^N|\mathbf{R}, \Theta)$. This leaves all time dependence in the probability of the object, while the bath relaxes instantaneously, following adiabatically the object configuration. This separation of timescales is characterized by the dimensionless parameter $\epsilon = \sqrt{\gamma/D_r M}$, which is small in the limit of massive objects. Following established procedures [17, 40], we integrate out the bath degrees of freedom to obtain underdamped Langevin dynamics for the object:

$$\begin{bmatrix} \dot{\mathbf{P}} \\ \dot{\mathbf{L}} \end{bmatrix} = \begin{bmatrix} \langle \mathbf{F} \rangle_b \\ \langle \Gamma \rangle_b \end{bmatrix} - \underbrace{\begin{bmatrix} \zeta_{PP} & \zeta_{PL} \\ \zeta_{LP} & \zeta_{LL} \end{bmatrix}}_{\zeta} \begin{bmatrix} \frac{1}{M} \mathbf{P} \\ \frac{1}{I} L \end{bmatrix} + \underbrace{\begin{bmatrix} \xi_P(t) \\ \xi_L(t) \end{bmatrix}}_{\xi}. \quad (3)$$

The bath produces three effects on the object: a mean force $\langle \mathbf{F} \rangle_b$ and torque $\langle \Gamma \rangle_b$, where $\langle \cdot \rangle_b$ denotes an average at fixed object configuration, an instantaneous friction ζ , and a white noise ξ . In this framework, the nine coefficients entering the friction matrix ζ are given by an Agarwal formula [43]

$$\zeta = \int_0^\infty dt \begin{bmatrix} \langle \delta \mathbf{F}(t) \nabla_{\mathbf{R}} \ln \rho_b(0) \rangle_b & \langle \delta \mathbf{F}(t) \partial_\Theta \ln \rho_b(0) \rangle_b \\ \langle \delta \Gamma(t) \nabla_{\mathbf{R}} \ln \rho_b(0) \rangle_b & \langle \delta \Gamma(t) \partial_\Theta \ln \rho_b(0) \rangle_b \end{bmatrix}, \quad (4)$$

where $\delta \mathbf{F} = \mathbf{F} - \langle \mathbf{F} \rangle_b$ and $\delta \Gamma = \Gamma - \langle \Gamma \rangle_b$. The three Gaussian noises are characterized by their correlation matrix λ , defined from

$$\langle \xi(t) \otimes \xi(t') \rangle = \lambda \delta_+(t - t') + \lambda^T \delta_-(t - t'), \quad (5)$$

where δ_\pm is the restriction of the Dirac function to \mathbb{R}_\pm and λ satisfies the Green-Kubo formula

$$\lambda = \int_0^\infty dt \begin{bmatrix} \langle \delta \mathbf{F}(t) \delta \mathbf{F}(0) \rangle_b & \langle \delta \mathbf{F}(t) \delta \Gamma(0) \rangle_b \\ \langle \delta \Gamma(t) \delta \mathbf{F}(0) \rangle_b & \langle \delta \Gamma(t) \delta \Gamma(0) \rangle_b \end{bmatrix}. \quad (6)$$

Equations (3)-(4) provide the most general dynamics for a rigid body in a chiral active bath, within the adiabatic approximation. They hold in any dimension $d \geq 2$ but neglect long-time tails due to conservation laws [44, 45], that can play an important role in low-dimensional active systems [41]. The object dynamics is then entirely defined by the sole knowledge of ζ , λ , and the ratchet forces, $\langle \mathbf{F} \rangle_b$ and $\langle \Gamma \rangle_b$, which are determined by the object shape. We now apply these theoretical results to demonstrate how the object departs from an effective equilibrium limit as its symmetry decreases.

The $SO(2)$ swirling disk. We begin by considering a circular disk, which has only translational degrees of freedom. By symmetry, $\langle \mathbf{F} \rangle_b = \mathbf{0}$, and the object dynamics reduce to

$$\dot{\mathbf{R}} = M^{-1} \mathbf{P}, \quad \dot{\mathbf{P}} = -M^{-1} \zeta_{PP} \mathbf{P} + \xi_P(t). \quad (7)$$

The combined isotropy of the bath and the disk make ζ and λ belong to the space of isotropic 2×2 matrices, which is spanned by $\delta = \begin{bmatrix} 1 & 0 \\ 0 & 1 \end{bmatrix}$ and $\mathbf{A} = \begin{bmatrix} 0 & -1 \\ 1 & 0 \end{bmatrix}$, so that $\zeta_{PP} = \zeta_{\parallel} \delta + \zeta_{\perp} \mathbf{A}$ and $\lambda_{PP} = \lambda_{\parallel} \delta + \lambda_{\perp} \mathbf{A}$. Here,

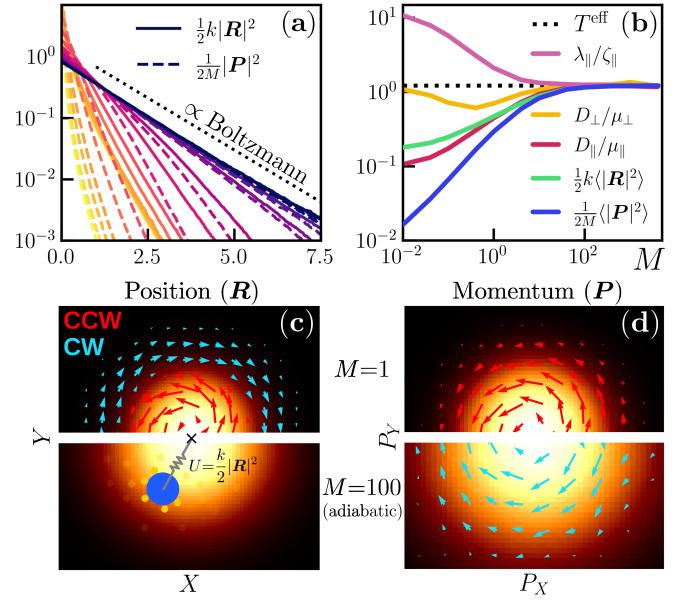


FIG. 2. **Confined disk: effective equilibrium and circulating momentum currents** ($\ell_p = 10$, $\ell_g = 5$). (a) The disk's potential (solid) and kinetic (dashed) energies converge to the Boltzmann distribution in the adiabatic limit ($M \in [10^{-2}, 10^3]$ increasing from light to dark). (b) Even and odd thermometers, constructed from λ , ζ , \mathbf{D} , and μ , all converge to a single T^{eff} in the adiabatic limit. (c) Probability density $\rho_{\mathbf{R}}$ (heatmap) and flux $\mathbf{J}_{\mathbf{R}}^{\text{ss}}$ (arrows) of the confined disk (cartoon overlay). Steady circulating currents (top) vanish at large M (bottom) due to the odd Einstein relation (9). (d) $\rho_{\mathbf{P}}$ and $\mathbf{J}_{\mathbf{P}}^{\text{ss}}$ of the same system. Circulation persists even in the adiabatic limit. The direction of rotation, determined by competition between ζ_{\perp} and λ_{\perp} , reverses at smaller M .

ζ_{\parallel} and λ_{\parallel} are the usual friction and noise correlations, respectively. Their odd counterparts, ζ_{\perp} and λ_{\perp} , stem from the breaking of time-reversal and parity symmetry of the bath. As we show below, they allow for steady circulating currents that are the counterparts to those observed in confined chiral active matter [46–57].

To investigate these odd currents, we confine the disk using a harmonic potential $U(\mathbf{R}) = \frac{1}{2}k|\mathbf{R}|^2$, as shown in Fig. 2. (Our results extend directly to more general potentials.) The simulations in Fig. 2a show how the nonequilibrium dynamics of light disks are replaced at large M by an effective equilibrium one, leading to the Boltzmann steady-state solution of Eq. (7) given by

$$\rho_o^{\text{ss}} = \rho_{\mathbf{R}}(\mathbf{R})\rho_{\mathbf{P}}(\mathbf{P}) \propto e^{-(U(\mathbf{R}) + \frac{1}{2M}|P|^2)/T^{\text{eff}}}, \quad (8)$$

where $T^{\text{eff}} = \frac{1}{2M}\langle |P|^2 \rangle = \frac{1}{2}k\langle |R|^2 \rangle$ is an effective temperature.

The flux in \mathbf{R} -space is $\mathbf{J}_{\mathbf{R}}^{\text{ss}} = -(\mathbf{D} - T^{\text{eff}}\mu)\nabla_{\mathbf{R}}\rho_{\mathbf{R}}$, where $\mathbf{D} = D_{\parallel}\delta + D_{\perp}\mathbf{A}$ is the diffusivity computed from the Green-Kubo relation $\mathbf{D} = \frac{1}{M^2}\int_0^\infty dt \langle \mathbf{P}(t)\mathbf{P}(0) \rangle$. The odd diffusivity D_{\perp} generates a flux of $\rho_{\mathbf{R}}$ perpendicular to its gradient [32]. Conversely, the mobility $\mu = \mu_{\parallel}\delta + \mu_{\perp}\mathbf{A} = \zeta^{-1}$ predicts the drift under an ex-

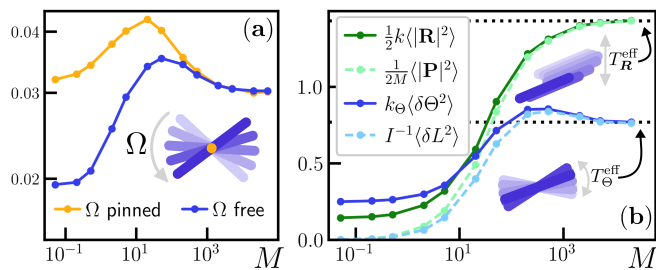


FIG. 3. **Effective temperatures of the spinning rod** ($\ell_{\text{rod}} = 5$, $\ell_p = 10$, and $\ell_g = 5$). (a) The angular velocities of rods pinned at the center or free to translate agree at large M . (b) A rod confined to a harmonic potential exhibits rotational (blue) and translational (green) dynamics that independently recover equilibrium-like statistics at large M , with the mean potential (solid) and kinetic (dashed) energies agreeing, but at two distinct effective temperatures T_R^{eff} and T_Θ^{eff} .

ternal force \mathbf{F}^{ext} as $\langle \mathbf{P} \rangle_{\mathbf{F}^{\text{ext}}} = M\boldsymbol{\mu}\mathbf{F}^{\text{ext}}$, where the odd mobility μ_\perp causes drift perpendicular to \mathbf{F}^{ext} [34, 35], and is maximal when the disk diameter is of the order ℓ_g (see Fig. 6 below). Einstein relations then follow as

$$D_\parallel = T^{\text{eff}}\mu_\parallel, \quad D_\perp = T^{\text{eff}}\mu_\perp, \quad (9)$$

remarkably holding for the odd parts as well as the even. Thus, while D_\perp and μ_\perp can individually drive currents satisfying $\nabla_{\mathbf{R}} \cdot \mathbf{J}_{\mathbf{R}}^{\text{ss}} = 0$, these exactly cancel at large M , as shown in Fig. 2c (bottom panel), leading to an effective equilibrium apparently reminiscent to that observed for a bath of achiral particles [17]. In contrast, when M is small, the disk departs from the equilibrium distribution of Eq. (8). The competition between D_\perp and μ_\perp then results in steady flows illustrated in Fig. 2c (top panel).

In the adiabatic limit, the flux of $\rho_{\mathbf{P}}$ is $\mathbf{J}_{\mathbf{P}}^{\text{ss}} = -(\boldsymbol{\lambda} - T^{\text{eff}}\boldsymbol{\zeta})\nabla_{\mathbf{P}}\rho_{\mathbf{P}}$. The continuity condition $\nabla_{\mathbf{P}} \cdot \mathbf{J}_{\mathbf{P}}^{\text{ss}} = 0$ requires that the even parts of $\boldsymbol{\lambda}$ and $\boldsymbol{\zeta}$ be related by a second fluctuation-dissipation theorem, but places no such requirement on the odd parts:

$$\lambda_\parallel = T^{\text{eff}}\zeta_\parallel, \quad \lambda_\perp \neq T^{\text{eff}}\zeta_\perp. \quad (10)$$

The inequality in Eq. (10) results in odd currents that persist even in the adiabatic limit (Fig. 2d), and can even change direction as the disk mass is decreased. This is in sharp contrast with both chiral equilibrium baths, which require $\lambda_\perp = T^{\text{eff}}\zeta_\perp$, and achiral active ones [17].

We stress that Eqs (8)-(10) provide independent thermometers to measure the effective temperature of the system. As shown in Fig. 2b, they all agree in the adiabatic limit. All involved quantities remain well-defined even beyond this limit, and are of rheological interest [58, 59], but cease to be directly connected through an effective temperature.

The C_2 Spinning rod. We now proceed beyond the isotropic disk by considering a passive rod, pictured in Fig. 1b. While reflection symmetry is lost due to the bath

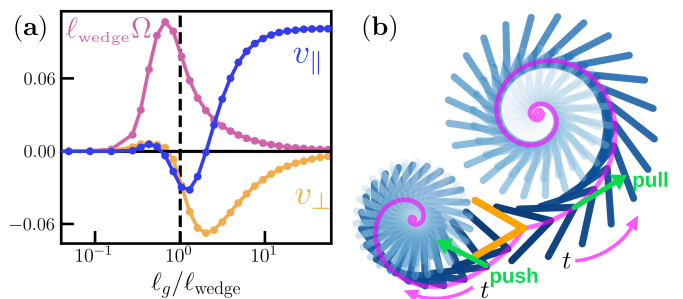


FIG. 4. **Nonequilibrium wedge dynamics** ($\ell_p = 10$, $\ell_{\text{wedge}} = 3.6$, $M = 100$). (a) Ratchet speeds $|v_\perp|$ and $|\Omega|$ are maximized at $\ell_g \approx \ell_{\text{wedge}}$. (b) Average trajectories with $\ell_{\text{wedge}} = \ell_g$, conditioned on the initial position (orange) when pushed or pulled with $\mathbf{F}^{\text{ext}} = \pm 0.1\mathbf{u}(\Theta)$ (green arrows). Pink lines trace the tip path. Asymmetry of the two trajectories results from rotation-translation coupling in $\boldsymbol{\zeta}$.

chirality, the system maintains a two-fold rotational symmetry (C_2). Consequently, $\langle \mathbf{F} \rangle_{\text{b}} = 0$, a result that holds for any object with n -fold rotational symmetry (C_n). The bath chirality nevertheless drives asymmetric accumulation around the rod, leading to a net torque and a rotational ratchet behavior.

Furthermore, Eqs. (6)-(4) show the elements of $\boldsymbol{\zeta}$ and $\boldsymbol{\lambda}$ that couple rotational and translational motion to vanish under C_n symmetry. This decoupling means that the translational dynamics of the rod are structurally identical to those of the isotropic disk, while the rotational dynamics obeys

$$\dot{L} = \langle \Gamma \rangle_{\text{b}} - I^{-1}\zeta_{LL}L + \xi_L(t), \quad (11)$$

leading to a non-zero average angular velocity $\Omega = \langle \Gamma \rangle_{\text{b}}/\zeta_{LL}$. This unexpected independence between translational and rotational dynamics is demonstrated in Fig. 3a, where a rod pinned at its center is shown to spin at the same speed as an unpinned rod (only) in the adiabatic limit. The freely rotating rod is then Boltzmann-distributed as $\rho_{\text{o}}^{\text{ss}} \propto e^{-\delta L^2/2IT_{\Theta}^{\text{eff}}}$, where $\delta L = L - I\Omega$ and $T_{\Theta}^{\text{eff}} = I^{-1}\langle \delta L^2 \rangle$ is the rotational temperature.

Another consequence of the decoupling is that translational and rotational degrees of freedom are both equilibrated, but at different temperatures. The stationary distribution of a rod in a confining potential $U = \frac{1}{2}k|\mathbf{R}|^2 + \frac{1}{2}k_\Theta\Theta^2$ is

$$\rho_{\text{o}}^{\text{ss}} \propto e^{-\left(\frac{k}{2}|\mathbf{R}|^2 + \frac{1}{2M}|\mathbf{P}|^2\right)/T_R^{\text{eff}}} e^{-\left(\frac{k_\Theta}{2}\delta\Theta^2 + \frac{1}{2I}L^2\right)/T_\Theta^{\text{eff}}}, \quad (12)$$

where $\delta\Theta = \Theta - \langle \Gamma \rangle_{\text{b}}/k_\Theta$. As shown in Fig. 3b, the translational temperature T_R^{eff} is nearly twice as “hot” as T_Θ^{eff} , even in the adiabatic limit, where the translational and rotational degrees of freedom individually obey equipartition between kinetic and potential energies.

We note that the odd circulation in momentum space of the disk is associated with a nonzero entropy production rate, which diverges as $\sigma \propto 1/\epsilon$. Similarly, the

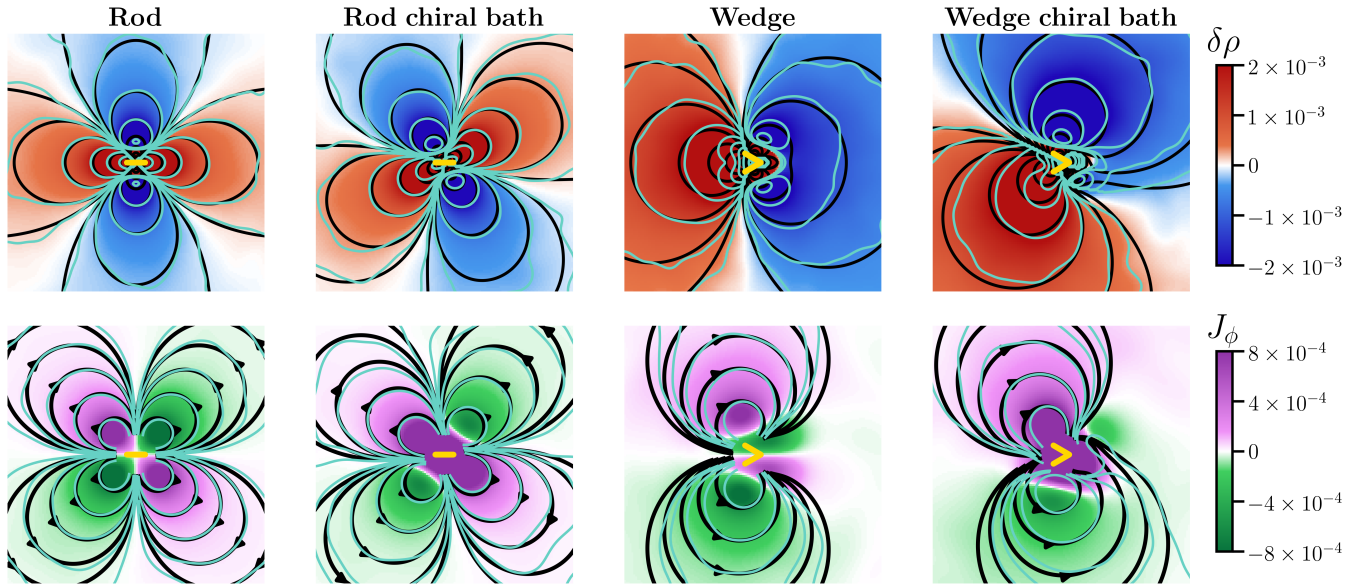


FIG. 5. **Far-field density and currents.** Top row: Steady-state density (heatmap and blue contour lines) compared against the multipole prediction (black contour lines). Bottom row: Steady-state current (blue streamlines) and heatmap of the rotational component $J_\phi = \mathbf{r} \times \mathbf{J}/|\mathbf{r}|$ compared against multipole prediction (black streamlines). First and third columns: achiral ($\ell_p = 10, \ell_g = \infty$). Second and fourth columns: chiral ($\ell_p = 10, \ell_g = 10$).

ratchet rotation of the rod leads to $\sigma = \frac{\langle \Gamma \rangle_b \Omega}{T_{\text{eff}}}$. These results seem to contradict the equilibrium-like statistics of Eq. (8) for the disk and of Eq. (11) for the rod. However, this paradox is resolved by noting that statistical reversibility is restored for objects with C_n symmetries under combined time reversal and chirality inversion ($\omega_0 \rightarrow -\omega_0$). As we now show, this is entirely lost when the object symmetry is further reduced.

The \mathbb{Z}_2 Steering wedge. A wedge, pictured in Fig. 1c, has no C_n symmetry, and its \mathbb{Z}_2 reflection symmetry is broken by the bath chirality. It thus experiences net forces and torques from the bath, behaving as both a rotational and translational ratchet with average velocities $v_{\parallel} = M^{-1} \langle \mathbf{u}(\Theta) \cdot \mathbf{P} \rangle$ and $v_{\perp} = M^{-1} \langle \mathbf{A} \mathbf{u}(\Theta) \cdot \mathbf{P} \rangle$, where $\mathbf{u}(\Theta) = [\cos(\Theta), \sin(\Theta)]^T$. In the achiral limit ($\ell_g \rightarrow \infty$) Ω and v_{\perp} vanish by symmetry. In the opposite limit ($\ell_g \rightarrow 0$) the active force f_0 acts over a vanishing small distance, and all three ratchet currents vanish. Consequently, Ω and v_{\perp} are maximal at intermediate values of ℓ_g which Fig. 4a shows to be selected for by the wedge size, ℓ_{wedge} . Note that, while a wedge always propels towards its tip in an achiral active bath, v_{\parallel} reverses at $\ell_g \approx \ell_{\text{wedge}}$, propelling in the opposite direction.

The lack of C_n symmetry of the wedge implies that rotational and translational motion are coupled in $\boldsymbol{\lambda}$ and $\boldsymbol{\zeta}$. This is illustrated in Fig. 4b, where the average trajectory of the wedge subject to “pulling” in the direction $\mathbf{u}(\Theta)$ or “pushing” in the opposite direction produces asymmetric trajectories with different directions of rotation. Unlike for the disk and rod, this coupling prevents defining effective rotational and translational tempera-

tures for the wedge, even in the adiabatic limit, where the entropy production is positive even under the symmetrization $\omega_0 \rightarrow -\omega_0$.

The bath’s perspective. Decreasing the object symmetry thus drives its dynamics increasingly far from equilibrium. This raises the question as to how the broken object symmetries influence the structure and flows of the bath itself. To answer that question, we characterize the universal far-field flow generated by the object in the chiral bath, building on a procedure developed for achiral baths [60, 61]. Far from the object, the bath dynamics is diffusive, obeying $\mathbf{J}_D = -\mathbf{D}^b \nabla \rho$, where $\rho(\mathbf{r})$ is the bath density and $\mathbf{D}^b = D_{\parallel}^b \boldsymbol{\delta} + D_{\perp}^b \mathbf{A}$ is the bath diffusivity. Near the object, in contrast, the flux \mathbf{J} of the active bath involves higher orientational moments. Defining $\delta \mathbf{J} = \mathbf{J} - \mathbf{J}_D$ and applying the steady-state continuity condition $\nabla \cdot \mathbf{J} = 0$ yields a Poisson equation for the density

$$D_{\parallel}^b \nabla^2 \rho = -\nabla \cdot \delta \mathbf{J}, \quad (13)$$

where $\nabla \cdot \delta \mathbf{J}$ acts as a localized source term. Equation (13) admits a multipole expansion in powers of the distance \mathbf{r} to the object that leads to

$$\rho(\mathbf{r}) = \rho_0 + \frac{1}{2\pi\gamma D_{\parallel}} \left\{ \frac{\mathbf{p} \cdot \mathbf{r}}{r^2} + \frac{\mathbf{r} \cdot \mathbf{q} \cdot \mathbf{r}}{2r^4} \right\} + \mathcal{O}(r^{-3}), \quad (14)$$

where ρ_0 is the bath density far from the object, and the

dipole and quadrupole moments are

$$\mathbf{p} = - \int d\mathbf{r} \rho(\mathbf{r}) \nabla V(\mathbf{r}), \quad (15)$$

$$\tilde{\mathbf{q}} = -2 \int d\mathbf{r} \rho(\mathbf{r}) \mathbf{r} \nabla V + \frac{2\gamma}{f_0} \mathbf{D}^b \mathbf{m}(\mathbf{r}) \nabla V. \quad (16)$$

Here, $\nabla V(\mathbf{r}_i) = -\mathbf{F}_i$ in Eq. (1), and $\mathbf{m}(\mathbf{r})$ is the polar order field, quantifying the orientational order of the bath. Note that the integrands in Eqs. (15)-(16) vanish everywhere except at the object, where $\nabla V \neq 0$. Plugging Eq. (14) into $\mathbf{J} = -\mathbf{D}^b \nabla \rho$ leads to an expression for the far-field flux,

$$\mathbf{J} \simeq -\frac{1}{2\pi\gamma D_{\parallel}} \mathbf{D}^b (r^2 \delta - 2\mathbf{r} \otimes \mathbf{r}) \left(\frac{\mathbf{p}}{r^4} + \frac{2\mathbf{q} \cdot \mathbf{r}}{r^6} \right), \quad (17)$$

where \mathbf{q} is the symmetric part of $\tilde{\mathbf{q}}$. In Fig. 5, the densities and fluxes induced by the rod and wedge in both chiral and achiral active baths are successfully compared with our multipole approximation, which show that the chirality of the bath effectively rotates the far field distribution with respect to the object. The increased departure from equilibrium as the object symmetry is decreased is reflected that the wedge is dominated by its dipole moment,

while the rod's leading contribution is only quadrupolar. Finally, the rotational flux $J_{\phi} = \mathbf{r} \times \mathbf{J}/|\mathbf{r}|$ of the chiral bath is observed to exhibit a large net circulation near the object. This is related to the torque on the object through Eq. (16), showing these effects to be two sides of the same coin.

Tayloring transport. Our results show how a passive object in contact with a chiral active bath turns into a chiral active particle, whose large-scale properties are determined by its *shape*, *mass*, and *size*. First, the object's symmetry determines which active ratchet behaviors and transport couplings are triggered, thus determining the nature of this effective active particle. Second, we have shown how to build a Langevin description of a heavy object, that predicts effective equilibrium descriptions albeit with odd signatures of nonequilibrium. Finally, our simulations show how tuning the object size to the bath gyroradius ℓ_g maximizes the odd response coefficients and chiral ratchet motion. An exciting perspective is now to explore the interactions between multiple objects mediated by chiral active bath and the possibility of Tayloring their self-assembly.

Acknowledgements. CH, FG, JT and FvW acknowledge the financial support of the ANR THEMA AAPG2020 grant.

-
- [1] X.-L. Wu and A. Libchaber, Phys. Rev. Lett. **84**, 3017 (2000).
- [2] D. Loi, S. Mossa, and L. F. Cugliandolo, Physical Review E **77**, 051111 (2008).
- [3] P. T. Underhill, J. P. Hernandez-Ortiz, and M. D. Graham, Phys. Rev. Lett. **100**, 248101 (2008).
- [4] K. C. Leptos, J. S. Guasto, J. P. Gollub, A. I. Pesci, and R. E. Goldstein, Phys. Rev. Lett. **103**, 198103 (2009).
- [5] J. Dunkel, V. B. Putz, I. M. Zaid, and J. M. Yeomans, Soft Matter **6**, 4268 (2010).
- [6] H. Kurtuldu, J. S. Guasto, K. A. Johnson, and J. P. Gollub, Proc. Natl. Acad. Sci. U.S.A **108**, 10391 (2011).
- [7] G. Foffano, J. S. Lintuvuori, K. Stratford, M. E. Cates, and D. Marenduzzo, Phys. Rev. Lett. **109**, 028103 (2012).
- [8] G. L. Miño, J. Dunstan, A. Rousselet, E. Clément, and R. Soto, J. Fluid Mech. **729**, 423 (2013).
- [9] A. Morozov and D. Marenduzzo, Soft Matter **10**, 2748 (2014).
- [10] E. W. Burkholder and J. F. Brady, Phys. Rev. E **95**, 052605 (2017).
- [11] S. Chaki and R. Chakrabarti, Phys. A Stat. Mech. its Appl. **511**, 302 (2018).
- [12] K. Kanazawa, T. G. Sano, A. Cairoli, and A. Baule, Nature **579**, 364 (2020).
- [13] M. Knežević and H. Stark, New J. Phys. **22**, 113025 (2020).
- [14] J. Reichert, L. F. Granz, and T. Voigtmann, Eur. Phys. J. E **44**, 27 (2021).
- [15] C. Maes, Phys. Rev. Lett. **125**, 208001 (2020).
- [16] O. Granek, Y. Kafri, and J. Tailleur, Physical Review Letters **129** (2022), 10.1103/PhysRevLett.129.038001.
- [17] A. Solon and J. M. Horowitz, Journal of Physics A: Mathematical and Theoretical **55** (2022), 10.1088/1751-8121/ac5d82.
- [18] B. Sorkin, H. Diamant, G. Ariel, and T. Markovich, Physical Review Letters **133**, 267101 (2024).
- [19] M. O. Magnasco, Physical Review Letters **71**, 1477 (1993).
- [20] C. Van den Broeck, R. Kawai, and P. Meurs, Physical review letters **93**, 090601 (2004).
- [21] L. Angelani, A. Costanzo, and R. Di Leonardo, Europhysics Letters **96**, 68002 (2011).
- [22] A. Gnoli, A. Petri, F. Dalton, G. Pontuale, G. Gradenigo, A. Sarracino, and A. Puglisi, Physical review letters **110**, 120601 (2013).
- [23] C. O. Reichhardt and C. Reichhardt, Annual Review of Condensed Matter Physics **8**, 51 (2017).
- [24] S. Krishnamurthy, S. Ghosh, D. Chatterji, R. Ganapathy, and A. Sood, Nature Physics **12**, 1134 (2016).
- [25] R. Zakine, A. Solon, T. Gingrich, and F. Van Wijland, Entropy **19**, 193 (2017).
- [26] P. Pietzonka, É. Fodor, C. Lohrmann, M. E. Cates, and U. Seifert, Physical Review X **9**, 041032 (2019).
- [27] É. Fodor and M. E. Cates, Europhysics Letters **134**, 10003 (2021).
- [28] R. Di Leonardo, L. Angelani, D. Dell'Arciprete, G. Ruocco, V. Iebba, S. Schippa, M. P. Conte, F. Mecarini, F. De Angelis, and E. Di Fabrizio, Proceedings of the National Academy of Sciences **107**, 9541 (2010).
- [29] A. Sokolov, M. M. Apodaca, B. A. Grzybowski, and I. S. Aranson, Proceedings of the National Academy of

- Sciences **107**, 969 (2010).
- [30] S. Anand, X. Ma, S. Guo, S. Martiniani, and X. Cheng, “Transport and Energetics of Bacterial Rectification,” (2024), arXiv:2308.08421 [cond-mat].
- [31] J.-R. Li, W.-j. Zhu, J.-J. Li, J.-C. Wu, and B.-Q. Ai, *New Journal of Physics* **25**, 043031 (2023).
- [32] C. Hargus, J. M. Epstein, and K. K. Mandadapu, *Physical Review Letters* **127**, 178001 (2021).
- [33] E. Kalz, H. D. Vuijk, I. Abdoli, J. U. Sommer, H. Löwen, and A. Sharma, *Physical Review Letters* **129**, 090601 (2022), 2206.13566.
- [34] C. Reichhardt and C. J. O. Reichhardt, *Physical Review E* **100**, 012604 (2019), arXiv:1901.11107.
- [35] A. R. Poggioli and D. T. Limmer, *Physical Review Letters* **130**, 158201 (2023).
- [36] A. P. Petroff, X.-L. Wu, and A. Libchaber, *Physical review letters* **114**, 158102 (2015).
- [37] K. Drescher, K. C. Leptos, I. Tuval, T. Ishikawa, T. J. Pedley, and R. E. Goldstein, *Physical review letters* **102**, 168101 (2009).
- [38] T. H. Tan, A. Mietke, J. Li, Y. Chen, H. Higinbotham, P. J. Foster, S. Gokhale, J. Dunkel, and N. Fakhri, *Nature* **607**, 287 (2022).
- [39] E. S. Bililign, F. Balboa Usabiaga, Y. A. Ganan, A. Poncet, V. Soni, S. Magkiriadou, M. J. Shelley, D. Bartolo, and W. T. Irvine, *Nature Physics* **18**, 212 (2022).
- [40] N. Van Kampen and I. Oppenheim, *Physica A: Statistical Mechanics and its Applications* **138**, 231 (1986).
- [41] O. Granek, Y. Baek, Y. Kafri, and A. P. Solon, *Journal of Statistical Mechanics: Theory and Experiment* **2020**, 1 (2020).
- [42] A. Jayaram and T. Speck, *Europhysics Letters* **143**, 17005 (2023).
- [43] G. S. Agarwal, *Zeitschrift für Physik A Hadrons and nuclei* **252**, 25 (1972).
- [44] H. van Beijeren, *Rev. Mod. Phys.* **54**, 195 (1982).
- [45] J. R. Dorfman, H. van Beijeren, and T. R. Kirkpatrick, *Contemporary kinetic theory of matter* (Cambridge University Press, 2021).
- [46] B. C. van Zuiden, J. Paulose, W. T. M. Irvine, D. Bartolo, and V. Vitelli, *Proceedings of the National Academy of Sciences* **113**, 12919 (2016), 1606.03934.
- [47] A. Souslov, B. C. van Zuiden, D. Bartolo, and V. Vitelli, *Nature Physics* **13**, 1091 (2017).
- [48] K. Dasbiswas, K. K. Mandadapu, and S. Vaikuntanathan, *Proceedings of the National Academy of Sciences of the United States of America* **115**, E9031 (2018), 1706.04526.
- [49] V. Soni, E. S. Bililign, S. Magkiriadou, S. Sacanna, D. Bartolo, M. J. Shelley, and W. T. M. Irvine, *Nature Physics* **15**, 1188 (2019).
- [50] Q. Yang, H. Zhu, P. Liu, R. Liu, Q. Shi, K. Chen, N. Zheng, F. Ye, and M. Yang, *Physical Review Letters* **126**, 198001 (2021).
- [51] H. D. Vuijk, J. U. Sommer, H. Merlitz, J. M. Brader, and A. Sharma, *Physical Review Research* **2**, 013320 (2020), 1908.02577.
- [52] E. Kalz, H. D. Vuijk, J.-U. Sommer, R. Metzler, and A. Sharma, *Physical Review Letters* **132**, 057102 (2024).
- [53] F. Vega Reyes, M. A. López-Castaño, and Á. Rodríguez-Rivas, *Communications Physics* **5**, 1 (2022), 2202.08920.
- [54] L. Caprini and U. M. B. Marconi, *Soft Matter* **15**, 2627 (2019).
- [55] L. Caprini, H. Löwen, and U. M. B. Marconi, *Soft Matter* **19**, 6234 (2023).
- [56] H. Li, H. Chaté, M. Sano, X.-q. Shi, and H. P. Zhang, *Physical Review X* **14**, 041006 (2024).
- [57] R. Wittmann, I. Abdoli, A. Sharma, and J. M. Brader, (2024), 10.48550/arXiv.2410.21087, 2410.21087.
- [58] D. Saintillan, *Annual Review of Fluid Mechanics* **50**, 563 (2018).
- [59] J. Shea, G. Jung, and F. Schmid, *Soft Matter* **20**, 1767 (2024).
- [60] Y. Baek, A. P. Solon, X. Xu, N. Nikola, and Y. Kafri, *Physical Review Letters* **120**, 1 (2018).
- [61] O. Granek, Y. Kafri, M. Kardar, S. Ro, J. Tailleur, and A. Solon, *Reviews of Modern Physics* **96**, 031003 (2024).
- [62] S. J. Plimpton, *Journal of computational physics* **117**, 1 (1995), see also <http://lammps.sandia.gov/>.
- [63] Simulation and analysis code is publicly available, www.github.com/chargus/chiral-active-bath.

End Matter

Simulation details. Molecular dynamics simulations were carried out using the LAMMPS simulation environment [62] with custom modifications [63] for the dynamics of the chiral active bath. The bath particles interact with the object through the purely repulsive Weeks-Chandler-Andersen (WCA) potential defined by

$$V(\mathbf{r}) = \begin{cases} 4\epsilon \left[(\sigma/\mathbf{r})^{12} - (\sigma/\mathbf{r})^6 \right] + \epsilon & |\mathbf{r}| < 2^{1/6}\sigma \\ 0 & |\mathbf{r}| \geq 2^{1/6}\sigma \end{cases} \quad (18)$$

with $\sigma = \epsilon = 1$. The total interaction energy is then $V^{\text{int}} = \sum_{i=1}^N \sum_{j=1}^{M_{\text{object}}} V(|\mathbf{r}_i - \mathbf{R}_j|)$, where the passive object (in the case of the rod and wedge) is constructed out of M_{object} point particles spaced at intervals of 0.1σ . The total force on the object is then $\mathbf{F} = -\sum_{j=1}^{M_{\text{object}}} \frac{\partial}{\partial \mathbf{R}_j} V^{\text{int}}$.

The passive object dynamics of Eq. (1) were integrated using the velocity Verlet algorithm while the stochastic dynamics of the bath in Eq. (2) were treated with a first-order Euler-Maruyama integrator, with a timestep of $\delta t = 0.005$. For the self-propulsion force and bath friction we set $f_0 = \gamma = 1$, so that the ℓ_p and ℓ_g are always adjusted by changing D_r and ω_0 .

The disk was harmonically confined by $U = \frac{1}{2}k|\mathbf{R}|^2$ with $k = 0.08$. Radial profiles of the steady-state fluxes are plotted in Fig. 6. The disk mobility $\mu = \zeta^{-1}$ was measured by pulling with an external force $|\mathbf{F}^{\text{ext}}| = 0.1$. The rod was harmonically confined by $U = \frac{1}{2}k|\mathbf{R}|^2 + \frac{1}{2}k_{\Theta}\Theta^2$ with $k = 2$ and $k_{\Theta} = 5$, which was sufficient to prevent any net rotation of the rod. The length of the rod and of the arms of the wedge (set at an angle of $\pi/3$)

were fixed at $\ell_{\text{rod}} = \ell_{\text{wedge}} = 10$. All calculations were performed in a simulation box with periodic boundaries and size 100×100 , except for the multipole calculations where a larger size of 300×300 was used to sample the

far-field effects. In those simulations, Ewald summation was used with a screening length of $\alpha = 1/300$ to account for the non-converging contribution of periodic images to the dipole contribution to $\rho(\mathbf{r})$, which decays as $1/|\mathbf{r}|$.

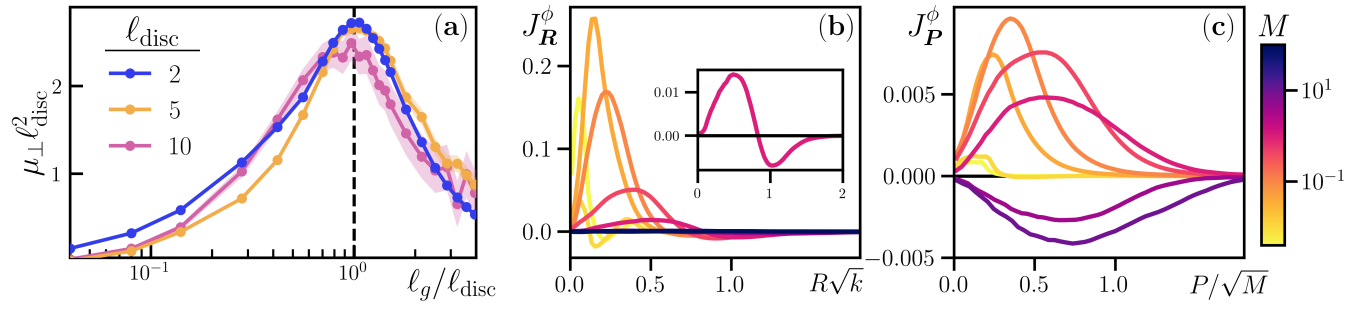


FIG. 6. **(a)** The odd mobility μ_{\perp} is maximized when the gyroradius ℓ_g of the bath is of the order of the disk diameter ℓ_{disc} . Error bands give 95% confidence interval from independent replicas of pulling simulations. **(b)** Profiles of the steady-state rotational currents in position space $J_{\mathbf{R}}^{\phi} = \mathbf{R} \times \mathbf{J}_{\mathbf{R}}^{\text{ss}} / |\mathbf{R}|$ and **(c)** momentum space $J_{\mathbf{P}}^{\phi} = \mathbf{P} \times \mathbf{J}_{\mathbf{P}}^{\text{ss}} / |\mathbf{P}|$ corresponding to Fig. 2c,d for various values of M . The inset in (b) shows the $M = 1$ profile plotted in Fig. 2c, emphasizing counter-rotation.